J̶M PAPERS

Restricted Euler dynamics in free-surface turbulence

Yinghe Qi[1],†, Zhenwei Xu[1] and Filippo Coletti[1]

[1]Department of Mechanical and Process Engineering, ETH Zurich, 8092 Zurich, Switzerland

The small-scale velocity gradient is connected to fundamental properties of turbulence at the large scales. By neglecting the viscous and non-local pressure Hessian terms, we derive a restricted Euler model for the turbulent flow along an undeformed free surface and discuss the associated stable/unstable manifolds. The model is compared with the data collected by high-resolution imaging on the free surface of a turbulent water tank with negligible surface waves. The joint probability density function (p.d.f.) of the velocity gradient invariants exhibits a distinct pattern from the one in the bulk. The restricted Euler model captures the enhanced probability along the unstable branch of the manifold and the asymmetry of the joint p.d.f. Significant deviations between the experiments and the prediction are evident, however, in particular concerning the compressibility of the surface flow. These results highlight the enhanced intermittency of the velocity gradient and the influence of the free surface on the energy cascade.

Key words: waves/free-surface flows

1. Introduction

The spatial and temporal fluctuations at small scales in fluid turbulence, which are highly non-Gaussian and long-range correlated (Mordant, Lévêque & Pinton 2004*b*), are among the most complex and consequential phenomena in fluid mechanics. The velocity gradient, as well as the velocity increment between two points, is found to be highly intermittent with extreme events occurring more frequently as the Reynolds number increases (Yeung, Zhai & Sreenivasan 2015). One possible mechanism for the enhanced intermittency at small scales is related to the nonlinear self-amplification of the velocity gradient tensor $A_{ij} = \partial u_i / \partial x_j$ during its Lagrangian evolution, where u_i is the fluid velocity component in direction x_i. This process is directly linked to the classic energy cascade picture in

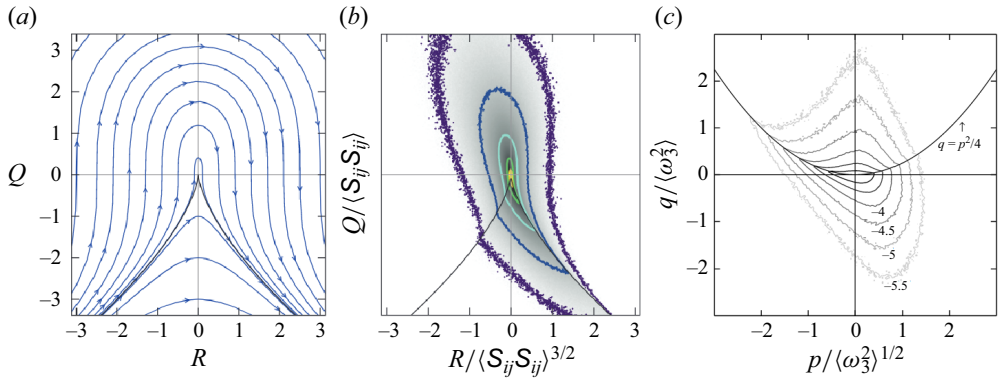† Email address for correspondence: yingqi@ethz.ch

Figure 1. (*a*) The Q–R trajectories of the restricted Euler model in 3-D turbulence. (*b*) The joint p.d.f. of Q and R of 3-D homogeneous and isotropic turbulence. Here, S_{ij} is the rate-of-strain tensor. Panels (*a,b*) are adapted with permission from Johnson & Wilczek (2024). (*c*) The joint p.d.f. of p and q along a 2-D section of 3-D turbulence. Panel (*c*) is adapted with permission from Cardesa *et al.* (2013).

turbulence in which large eddies are assumed to fragment into small eddies (Kolmogorov 1941) with energy transferring from large to small scales.

In addition to the intrinsic strong intermittency, further universal behaviours of A_{ij} include the negative skewness of the longitudinal velocity gradient (Sreenivasan & Antonia 1997), and the preferential alignment between vorticity and the eigenvector associated with the intermediate eigenvalue of the rate-of-strain tensor (Kerr 1985; Elsinga & Marusic 2010*b*; Xu, Pumir & Bodenschatz 2011). Moreover, the joint probability density function (p.d.f.) of the invariants $Q = -A_{ij}A_{ji}/2$ and $R = -A_{ij}A_{jk}A_{ki}/3$ is found to exhibit a universal teardrop shape (figure 1*b*), with higher probability along the Vieillefosse tail $27R^2/4 + Q^3 = 0$ (Vieillefosse 1982, 1984; Meneveau 2011) for various Reynolds number and flow configurations (Soria *et al.* 1994; Chong *et al.* 1998; Lüthi, Holzner & Tsinober 2009; Elsinga & Marusic 2010*a*; Lozano-Durán, Holzner & Jiménez 2016). These behaviours reflect fundamental processes involved in turbulent flows, e.g. vortex stretching and strain self-amplification.

Dynamic system models from a Lagrangian point of view provide a powerful tool to study the evolution of the velocity gradient and connect dynamics, statistics and structures of turbulence in a unified framework (Meneveau 2011; Johnson & Wilczek 2024). By taking the spatial gradient of the Navier–Stokes equation and neglecting the terms involving the viscous effect and anisotropic pressure Hessian, Vieillefosse (1982, 1984) and Cantwell (1992) derived the restricted Euler model,

$$\frac{\mathrm{d}A_{ij}}{\mathrm{d}t} + A_{ik}A_{kj} - (A_{km}A_{mk})\frac{\delta_{ij}}{3} = 0, \tag{1.1}$$

where δ_{ij} is the Kronecker delta function. Despite the simplifying assumptions, the restricted Euler model captures the self-amplification of the velocity gradient and is remarkably successful at predicting its aforementioned key features, including the teardrop shape observed in the joint p.d.f. of invariants. This model has further inspired subsequent works (Girimaji & Pope 1990; Chevillard & Meneveau 2006; Biferale *et al.* 2007; Chevillard *et al.* 2008; Wilczek & Meneveau 2014; Johnson & Meneveau 2016) which have attempted to obtain more accurate turbulent statistics by modelling the unclosed terms.

More recently, Cardesa *et al.* (2013) measured the 2×2 reduced velocity gradient tensor $\tilde{A}_{ij}$ along a two-dimensional (2-D) section of three-dimensional (3-D) turbulence.

The joint p.d.f. of velocity gradient invariants (p and q) exhibits a universal teapot pattern for various flow configurations, as illustrated in figure 1(c). Although the underlying mechanism leading to the teapot pattern is still not completely understood, the asymmetry of the pattern is found to be associated with the predominance of vortex stretching over compression in 3-D turbulence.

Despite the progress in the understanding and predicting the dynamics of A_{ij} in 3-D turbulence, insights of the reduced velocity gradient tensor $\tilde{A}_{ij}$ in free-surface turbulence, to our best knowledge, are still lacking. Here, we define $\tilde{A}_{ij}$ being the top left-hand 2×2 block of the full velocity gradient A_{ij}, with $i, j = 1, 2$ representing the surface-parallel directions. Here $\tilde{A}_{ij}$ is related to multiple fundamental features of free-surface turbulence, such as surface deformation (Babiker *et al.* 2023), compressible velocity field (Boffetta, De Lillo & Gamba 2004), exchange of mass between the free surface and the bulk (McKenna & McGillis 2004; Herlina & Wissink 2019) and its intermittent nature (Goldburg *et al.* 2001; Li *et al.* 2024). These features affect a variety of large-scale phenomena including the exchange of gas between the atmosphere and ocean (Jähne & Haußecker 1998; Veron 2015), the transport of oceanic pollutants such as microplastics (Zhang 2017; Mountford & Morales Maqueda 2019; van Emmerik & Schwarz 2020) and the blooming of phytoplankton (Durham *et al.* 2013; Lindemann, Visser & Mariani 2017). In this work, we developed a restricted Euler model for the reduced velocity gradient tensor $\tilde{A}_{ij}$ at an undeformed free surface, from which the dynamic equations of the invariants are obtained. This model provides new insights on various fundamental features of free-surface turbulence, including its enhanced intermittency observed in laboratory experiments. Deviations from the observations suggest directions to further improve the modelling framework. This paper is organized as follows. In § 2, we introduce the restricted Euler model for free-surface flows. This model is then compared with experimental data in § 3. Section 4 summarizes our findings and draws conclusions.

2. Restricted Euler model

We begin with adapting the restricted Euler model originally derived for 3-D turbulence (see (1.1)). For homogeneous and isotropic free-surface turbulence, the shear-free boundary condition on the free surface requires the derivative of horizontal velocity along the vertical direction to be zero, i.e. $\partial u_1 / \partial x_3 = \partial u_2 / \partial x_3 = 0$. We further focus on the situation in which the surface deformation is negligible, which is the case in a wide range of naturally occurring water flows (Brocchini & Peregrine 2001). Then, the no-penetration condition requires the vertical velocity on the free surface to also be zero, i.e. $u_3 = 0$. This further leads to $\partial u_3 / \partial x_1 = \partial u_3 / \partial x_2 = 0$. Combining both boundary conditions, we write

$$A_{13} = A_{23} = A_{31} = A_{32} = 0. \tag{2.1}$$

By setting $i, j = 1, 2$ while keeping $k, m = 1, 2, 3$ in (1.1), the restricted Euler model reduces to the transport equation for $\tilde{A}_{ij}$ which still contains terms such as A_{13} and A_{33}. By further applying the shear-free and no-penetration boundary conditions on the free surface (see (2.1)) and the incompressibility condition $A_{33} = -A_{11} - A_{22} = -\text{tr}(\tilde{A}_{ij})$, these terms are eliminated and (1.1) becomes the restricted Euler equation on the free surface:

$$\frac{\mathrm{d}\tilde{A}_{ij}}{\mathrm{d}t} + \tilde{A}_{ik}\tilde{A}_{kj} - (\tilde{A}_{km}\tilde{A}_{mk} + \tilde{A}_{nn}^2)\frac{\delta_{ij}}{3} = 0. \tag{2.2}$$

Equation (2.2) provides a simplified model for the Lagrangian evolution of the reduced velocity gradient tensor in non-wavy free-surface turbulence. Here, $\tilde{A}_{ik}\tilde{A}_{kj}$ is the nonlinear

self-amplification term that accounts for the enhanced intermittency, while the term $\tilde{A}_{nn}^2$ signals the role of the non-solenoidal nature of the surface flow.

Given the restricted Euler model for $\tilde{A}_{ij}$, the Lagrangian evolution equations for the invariants $p = -\text{tr}(\tilde{A}_{ij}) = -\tilde{A}_{11} - \tilde{A}_{22}$ and $q = \det(\tilde{A}_{ij}) = \tilde{A}_{11}\tilde{A}_{22} - \tilde{A}_{12}\tilde{A}_{21}$ can also be obtained. The dynamic equation for p is derived by taking the trace of (2.2), i.e.

$$\frac{\mathrm{d}p}{\mathrm{d}t} = -\frac{1}{3}p^2 - \frac{2}{3}q. \tag{2.3}$$

The dynamic equation for q can be obtained by multiplying equation (1.1) by A_{ij} and then applying the boundary condition on the free surface as well as the incompressibility condition. This leads to the transport equation for the double product term $\tilde{A}_{in}\tilde{A}_{nj}$, i.e.

$$\frac{\mathrm{d}\tilde{A}_{in}\tilde{A}_{nj}}{\mathrm{d}t} + 2\tilde{A}_{in}\tilde{A}_{nk}\tilde{A}_{kj} - \frac{2}{3}(\tilde{A}_{km}\tilde{A}_{mk} + \tilde{A}_{nn}^2)A_{ij} = 0. \tag{2.4}$$

In this equation, the triple product term $\tilde{A}_{in}\tilde{A}_{nk}\tilde{A}_{kj}$ can be rewritten using the Cayley–Hamilton theorem, $\tilde{A}_{in}\tilde{A}_{nk} + p\tilde{A}_{ik} + q\delta_{ik} = 0$, multiplied by $\tilde{A}_{kj}$ to reduce the triple product term to a double one. Then, taking the trace of the transport equation for $\tilde{A}_{in}\tilde{A}_{nj}$ and eliminating the resulting $\mathrm{d}p/\mathrm{d}t$ term using (2.3) leads to the dynamic equation for q:

$$\frac{\mathrm{d}q}{\mathrm{d}t} = -\frac{2}{3}p^3 + \frac{5}{3}pq. \tag{2.5}$$

Equations (2.3) and (2.5) form a 2-D nonlinear dynamic system for the evolution of the invariants. It is evident that there is only one fixed point at the origin $p = q = 0$. Through this fixed point, two manifolds exist and can be expressed as

$$q = p^2/4, \tag{2.6}$$

and

$$q = -2p^2. \tag{2.7}$$

The proof of these expressions can be found by comparing the gradient along the manifold, i.e. $\mathrm{d}q/\mathrm{d}p$ and $\mathrm{d}q/\mathrm{d}p$ calculated by the dynamic system. Evidently, both manifolds exhibit a parabolic form. Moreover, $q = p^2/4$ happens to be the boundary across which the eigenvalues of the reduced velocity gradient tensor $\tilde{A}_{ij}$ change from complex to real and the local flow topology changes between stable/unstable foci and stable/unstable nodes (see figure 2). As suggested by Cantwell (1992), this is coincidental: the factor $1/3$ in (1.1) is chosen so that the anisotropic pressure Hessian is zero; if a different factor is used, a distinct dynamic system with different manifolds is obtained. We also note that this coincidence is also observed in 3-D turbulence, in which the Vieillefosse tail (figure 1a) also happens to be the boundary that separates the real (corresponding to stable/unstable nodes in 3-D turbulence) and complex (stable/unstable foci) eigenvalues of the velocity gradient tensor.

It is interesting to examine the stability of these manifolds. For any arbitrary point $(p_0, p_0^2/4)$ located on the first manifold ($q = p^2/4$), the dynamics is determined by the Jacobian
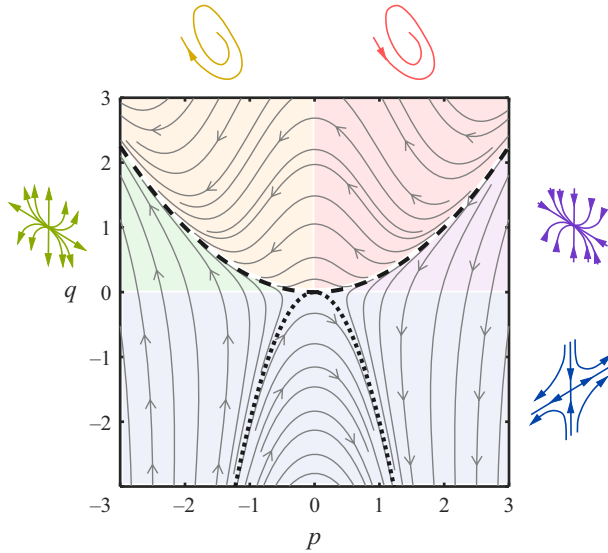
Figure 2. Restricted Euler trajectories (grey lines) calculated based on (2.3) and (2.5). The arrows mark the direction of the trajectories in the phase portrait. The black dashed line and the black dotted line denote the manifolds $q = p^2/4$ and $q = -2p^2$, respectively. The shades highlight the local flow topology in each region: stable foci (red); unstable foci (yellow); unstable node (green); saddle (blue); stable node (purple) (Perry & Chong 1987).

matrix of the dynamic system,

$$\boldsymbol{J} = \begin{bmatrix} \dfrac{\partial(\mathrm{d}p/\mathrm{d}t)}{\partial p} & \dfrac{\partial(\mathrm{d}p/\mathrm{d}t)}{\partial q} \\ \dfrac{\partial(\mathrm{d}q/\mathrm{d}t)}{\partial p} & \dfrac{\partial(\mathrm{d}q/\mathrm{d}t)}{\partial q} \end{bmatrix} = \begin{bmatrix} -\dfrac{2}{3}p_0 & -\dfrac{2}{3} \\ -\dfrac{19}{12}p_0^2 & \dfrac{5}{3}p_0 \end{bmatrix}. \tag{2.8}$$

We then examine the stability of this point along the normal direction with respect to the manifold, which is determined by calculating the term $\hat{e}_{\perp i} J_{ij} \hat{e}_{\perp j}$, where $\hat{e}_{\perp i}$ is the unit vector normal to the same manifold. The condition $\hat{e}_{\perp i} J_{ij} \hat{e}_{\perp j} > 0$ implies that $(p_0, p_0^2/4)$ is unstable, and *vice versa*. By substituting $q = p^2/4$ into $\hat{e}_{\perp i} J_{ij} \hat{e}_{\perp j}$, we can write $\hat{e}_{\perp i} J_{ij} \hat{e}_{\perp j} = (5p_0^2 + 16)(2p_0^2 + 8)^{-1} p_0$. Evidently, the sign of $\hat{e}_{\perp i} J_{ij} \hat{e}_{\perp j}$ is consistent with the sign of p_0. This indicates that the first manifold ($q = p^2/4$) is unstable for $p > 0$ and stable for $p < 0$. A similar analysis can be conducted for the other manifold $q = -2p^2$, and one can write $\hat{e}_{\perp i} J_{ij} \hat{e}_{\perp j} = -(32p_0^2 + 1)(16p_0^2 + 1)^{-1} p_0$. The sign of $\hat{e}_{\perp i} J_{ij} \hat{e}_{\perp j}$ is opposite to the sign of p_0, suggesting that this manifold is stable for $p > 0$ while is unstable for $p < 0$.

Figure 2 shows the p–q phase portrait based on the restricted Euler model calculated numerically from (2.3) and (2.5). The arrows indicate the directions in which the system evolves. Also shown are the two manifold $q = p^2/4$ and $q = -2p^2$. The trajectories above the parabola $q = p^2/4$ are directed from right to left with a bump around the axis $p = 0$, and move from left to right below the parabola $q = -2p^2$. The stability properties of the manifolds are evident by recognizing that the trajectories are directed towards or away from the manifolds depending on the sign of p, consistent with the analysis presented above. The phase portrait also suggests that all initial conditions will eventually proceed to a finite-time singularity along either the left-hand branch of $q = p^2/4$ or the right-hand branch of $q = -2p^2$. This finite-time singularity along $q = p^2/4$ corresponds

1002 A38-5

to the same singularity along the Vieillefosse tail in 3-D turbulence (see figure 1*a*) and thus they represent the same physical flow topology with different mathematical manifestations. The presence of finite-time singularities implies that *p* and *q*, as well as $\tilde{A}_{ij}$, will eventually approach infinity via a process of gradient self-amplification, as in 3-D turbulence (Meneveau 2011; Johnson & Wilczek 2024). In real flows, viscosity and the pressure Hessian will prevent diverging values of the velocity gradient. However, the presence of two manifolds associated with finite-time singularities suggests that extremely large values of velocity gradients are relatively likely, even more so than in 3-D turbulence. Indeed, simulations by Eckhardt & Schumacher (2001) and measurements by Li *et al.* (2024) emphasized how free-surface turbulence is characterized by stronger intermittency than 3-D turbulence.

The *p*–*q* phase portrait also predicts how the topology of the local velocity field evolves over time. As illustrated by the schematic and shade in figure 2, it can be seen that stable foci above $q = p^2/4$ in the first quadrant will evolve towards unstable foci. This is consistent with the dynamics in the 3-D restricted Euler system (see figure 1*a*) in which stable foci also evolve into unstable foci governed by $\mathrm{d}R/\mathrm{d}t = (2/3)Q^2 \geq 0$. Stable nodes below $q = p^2/4$ in the first quadrant will become saddles, while unstable nodes can only evolve from saddles. Saddles below $q = -2p^2$ remain such, thus their topology does not significantly change. These behaviours correspond to the intermediate eigenvalue of the three real eigenvalues of the full velocity gradient tensor changing from negative to positive, again equivalent to the dynamics in the 3-D restricted Euler system. We emphasize that this insight on the flow topology is based on the restricted Euler model in which the effects of viscosity and anisotropic pressure Hessian are removed.

3. Experimental set-up and results

To verify the prediction of the restricted Euler dynamics in free surface turbulence, we present results from experiments conducted in a turbulent water tank of dimensions $2 \times 1 \times 1\mathrm{m}^3$, illustrated in figure 3(*a*). Two 8×8 arrays of submerged pumps facing each other generate homogeneous turbulence in the centre of the tank over a region of approximately $(0.5 \ \mathrm{m})^3$. Details regarding this facility can be found in Ruth & Coletti (2024) and Li *et al.* (2024). The intensity of the velocity fluctuations u_{rms} and the dissipation rate of the turbulent kinetic energy ϵ are varied in the range $u_{rms} = 0.02$ to $0.03 \ \mathrm{m} \ \mathrm{s}^{-1}$ and $\epsilon = 3.82 \times 10^{-5}$ to $2.21 \times 10^{-4} \ \mathrm{m}^2 \ \mathrm{s}^{-3}$ by changing the power supplied to each pump. This leads to a range of Taylor Reynolds number $Re_\lambda = 207$ to 312. We note that strong surface deformation due to the subsurface turbulence could bring difficulties and large uncertainty in the surface velocity measurement. However, in this regime, the surface remains essentially flat, with only submillimetre deformations due to the subsurface turbulence. Therefore, such surface deformation is neglected and will not significantly affect the result.

The free surface of the water is maintained at 8 cm above the axis of the jets at the top row of the arrays. As depicted in figure 3(*a*), the surface motion is captured by a downward looking CMOS camera placed approximately 0.31 m above the surface. This is operated at 400 f.p.s., with a resolution of 1664×1600 pixels over a $10 \times 10 \ \mathrm{cm}^2$ FOV illuminated by two light-emitting diode panels. To resolve the small-scale dynamics, the surface motion is characterized by tracking floating hollow glass microspheres (63–75 μm in diameter and 0.31 g cm^{-3} in density), at a high concentration approximately 120 particles cm^{-2}. Individual particles are identified and tracked via an in-house particle tracking velocimetry (PTV) code based on the nearest-neighbour algorithm (Petersen,
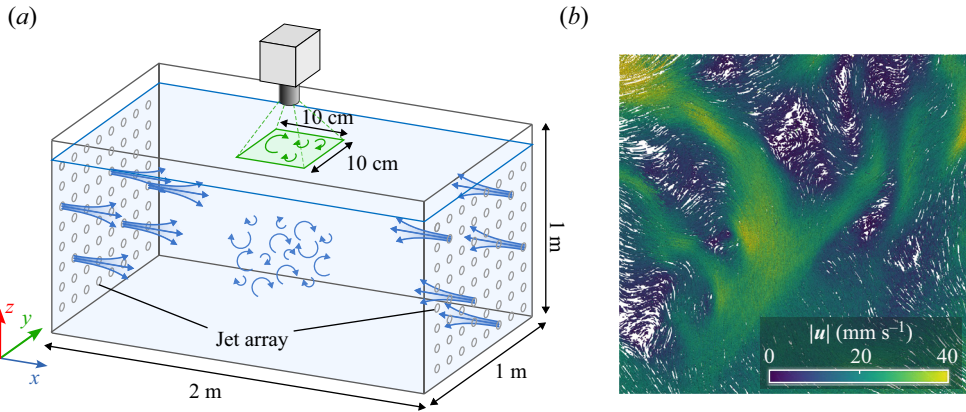
(*a*)   (*b*)

Figure 3. (*a*) A schematic of the turbulent water tank and camera arrangement. The green shaded area represents the field of view (FOV). (*b*) A snapshot of particle trajectories on the free surface in the FOV at $Re_\lambda = 312$. The trajectories are colour coded by the velocity magnitude.

Baker & Coletti 2019). The velocity is obtained by convolving the trajectories with the first derivative of a temporal Gaussian kernel, whose width is comparable to the smallest time scales of the flow (Mordant, Crawford & Bodenschatz 2004*a*). Figure 3(*b*) shows an example of trajectories obtained over a series of 25 successive images.

The reduced velocity gradient tensor $\tilde{A}_{ij}$ at each particle position on the free surface is obtained by performing a least-square fit based on the velocity of particles within a search radius R_s (Pumir, Bodenschatz & Xu 2013; Qi *et al.* 2022). When R_s is large, the calculated velocity gradient will be coarse-grained; while small R_s leads to a limited number of surrounding particles, thus larger uncertainty. The value is thus determined following an approach similar to the one for the PTV kernel (Mordant *et al.* 2004*a*): R_s is chosen as the smallest value above which the standard deviation of $\tilde{A}_{ij}$ decays exponentially with it. Following this approach, $R_s = 2.5$ mm is used which yields on average 40 particles within the search radius. This R_s is comparable to the Kolmogorov length scale defined on the free surface and the results are insensitive to the precise value of the search radius. More details can be found in Qi, Li & Coletti (2024).

With $\tilde{A}_{ij}$ obtained from the experiment, the invariants p and q are calculated and their joint p.d.f.s are shown in figure 4(*a*) for $Re_\lambda = 312$. Both invariants are normalized by the vorticity of the surface flow, $\omega = \tilde{A}_{21} - \tilde{A}_{12}$. The dashed line and dotted line mark the manifolds $q = p^2/4$ and $q = -2p^2$ obtained from the reduced Euler representation. We note the distribution of the joint p.d.f. does not change significantly between various cases. Thus, the following discussion should apply for at least the Reynolds number range considered in this work.

Remarkably, the contours in the *p*–*q* joint p.d.f. show similarities with the trajectories in the analytical phase portrait shown in figure 2. In particular, a relatively high probability is found along the manifold $q = p^2/4$, especially its left branch, highlighting the role of strain self-amplification which results in exceptionally strong intermittency. Quantitatively, the kurtosis of the velocity gradients along the surface ($\tilde{A}_{11}$) is approximately 9.5, which is higher than the one for 3-D homogeneous turbulence at similar Re_λ (Gylfason, Ayyalasomayajula & Warhaft 2004). The asymmetry of the distribution reflects the stability properties of this manifold, i.e. the left-hand branch is stable as discussed above and thus exhibits higher probability. Although the manifold $q = -2p^2$ does not leave an obvious footprint, the relatively higher probability in the fourth quadrant than the one in
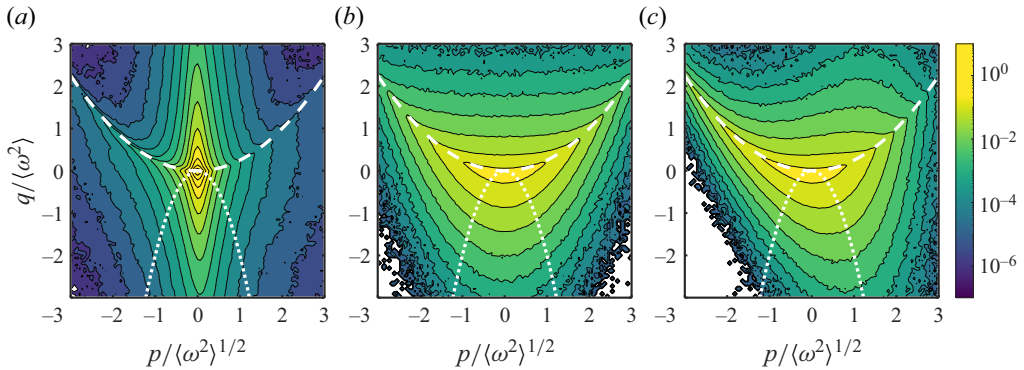
Figure 4. (*a*) The joint p.d.f. of normalized p and q at $Re_\lambda = 312$ based on the experimental data. The logarithmic contours range from 10^{-7} to 10 with adjacent contours being separated by half a decade. (*b*) The initial joint p.d.f. of normalized p and q for the Monte Carlo simulation. (*c*) The joint p.d.f. of normalized p and q obtained from the Monte Carlo simulation at $\langle\omega^2\rangle^{1/2}t = 0.15$. For (*b,c*), the logarithmic contours range from 10^{-6} to 1 with adjacent contours being separated by half a decade. In all the three panels, the white dashed lines mark $q = p^2/4$, and white dotted lines mark $q = -2p^2$.

the third quadrant is consistent with the stability of its right-hand branch. The fact that no clear tail is observed along this manifold still requires further investigation.

To better compare the joint p.d.f. with the restricted Euler model, a Monte Carlo simulation is performed. A large ensemble of $O(10^7)$ initial sets of invariants is considered and each of these sets is evolved following (2.3) and (2.5). The initial values of invariants are obtained from the reduced velocity gradient tensor, each element of which follows a Gaussian distribution with the same variance and zero mean, as illustrated in figure 4(*b*). We note that as the restricted Euler system is divergent, the predicted joint p.d.f. does not converge to a statistically stationary state. Thus, in figure 4(*c*), the predicted joint p.d.f. at an intermediate time instant ($\langle\omega^2\rangle^{1/2}t = 0.15$, where t indicates time) is used to compare with the experimental data, though the features remain qualitatively similar at different times.

In figure 4, large deviations between the experimental and the predicted joint p.d.f. are evident, in particular the high probability around $p = 0$ in the former. This is associated with low levels of the compressibility ratio $\mathcal{C} = \langle(\tilde{A}_{ii})^2\rangle/\langle(\tilde{A}_{ij})^2\rangle = 0.013$–0.024 found in the measurements. This is much lower than $\mathcal{C} = 0.45$–0.5 observed by Cressman *et al.* (2004) who forced turbulence at a much deeper distance under the free surface with $Re_\lambda = 100$–140. It is possible that differences in the details of the forcing scheme impact the state of the surface flow. We note, however, that the compressibility ratio we measure is largely unaffected by changing the depth of the forcing. Despite the large deviations, the predicted joint p.d.f. still successfully reproduces some features of the experimental data; in particular, the higher probability along the left-hand branch of $q = p^2/4$ and the slightly higher probability in the fourth quadrant than the one in the third quadrant. The manifold $q = -2p^2$ does not show a clear footprint as in the experimental data, indicating that this manifold might not affect the dynamics of the reduced velocity gradient as much as the manifold $q = p^2/4$.

Given the asymmetry observed in the measured joint p.d.f. (figure 4*a*), it is informative to examine the mean of both invariants. As the gradients of the mean velocity components are weak (Li *et al.* 2024), the average of p is expected to be approximately zero $\langle p \rangle = -\partial\langle u_1\rangle/\partial x_1 - \partial\langle u_2\rangle/\partial x_2 = 0$. In addition, given the homogeneity of the free-surface turbulence, the cross product of velocity gradient also satisfies $\langle(\partial u_1/\partial x_1)$

$(\partial u_2/\partial x_2)\rangle = \langle(\partial u_1/\partial x_2)(\partial u_2/\partial x_1)\rangle$ (George & Hussein 1991). Substituting this relation into the definition of q results in $\langle q\rangle = \langle(\partial u_1/\partial x_1)(\partial u_2/\partial x_2)\rangle - \langle(\partial u_1/\partial x_2)(\partial u_2/\partial x_1)\rangle = 0$. Therefore, both invariants are expected to have zero mean, $\langle p\rangle = \langle q\rangle = 0$. This is approximately confirmed by the present data, which gives $\langle p\rangle/\langle\omega^2\rangle^{1/2} = 1.7 \times 10^{-3}$ and $\langle q\rangle/\langle\omega^2\rangle = -0.035$.

It is also noted that the joint p.d.f. of invariants (figure 4*a*) displays a distinct pattern from the one obtained from generic 2-D sections of 3-D turbulence (Cardesa *et al.* 2013). The teapot shape (as in figure 1*c*) shows a much more pronounced asymmetry compared with the present free-surface case. This asymmetry, quantified by the inequality $\langle pq\rangle < 0$, is found to be connected to the predominance of vortex stretching over vortex compression in 3-D turbulence. In particular, they found that $\langle pq\rangle/\langle\omega^2\rangle^{3/2}$ ranged between -0.044 and -0.067 for 3-D turbulence, while in the present case we measure $\langle pq\rangle/\langle\omega^2\rangle^{3/2} = -1.8 \times 10^{-3}$. Therefore, we deduce that the weaker asymmetry observed here is due to the no-shear-stress boundary condition which eliminates the vortex stretching along the free-surface directions. This is crucial for the dynamics, as vortex stretching is a major factor in the interscale energy transfer in 3-D turbulence (Davidson 2015; Johnson 2020, 2021). This may have far-reaching consequences for the energy cascade associated with the dynamics along the free surface, which has been found to exhibit inverse interscale fluxes from scales small to large (Pan & Banerjee 1995; Lovecchio, Zonta & Soldati 2015). Moreover, surface-attached vortices are linked to surface-divergence events (Babiker *et al.* 2023) which are crucial for gas transfer to and from the liquid (Jähne & Haußecker 1998; Herlina & Wissink 2019). Inspired by these considerations, further studies are warranted to conduct a complete description of the surface flow topology and dynamics.

4. Conclusion

In this work, we have developed a restricted Euler model for the reduced velocity gradient tensor in free-surface turbulence by simplifying the 3-D restricted Euler model using free-surface boundary conditions. Two manifolds associated with finite-time singularities appear in the phase portrait that describes the dynamics of the invariants p and q, highlighting the intrinsic intermittent nature of $\tilde{A}_{ij}$. The model is compared with experimental data obtained in a turbulent water tank with quasiflat free surface, in which the surface velocity gradient is obtained by tracking highly concentrated floating microspheres. The p–q joint p.d.f. shows a distinct pattern which differs significantly from the one measured in 2-D sections of 3-D turbulence. Some features of the joint p.d.f., including the high probability along the unstable branch of $q = p^2/4$ and the asymmetry of the distribution, are predicted by the restricted Euler model. This study provides experimental evidence as well as a theoretical basis for the enhanced intermittency in free-surface turbulence.

Despite the success of the current model in predicting certain features, large deviations between the experimental and predicted joint p.d.f.s are evident, particularly the high probability around $p = 0$, associated with a weak surface compressibility observed in the experiments which deserves further investigation. In addition, the magnitude of the skewness is greatly overpredicted. We remark that the current model is inherently not convergent (i.e. does not reach a steady state) due to the lack of pressure Hessian and viscous effect. Further improvements of the model to take into account these terms are needed to guarantee convergent and more accurate predictions, and to advance the understanding on the evolution of the reduced velocity gradient tensor on the free surface.

Declaration of interests. The authors report no conflict of interest.

Data availability statement. All the data supporting this work are available from the corresponding author upon reasonable request.

Author ORCIDs.

- Yinghe Qi https://orcid.org/0009-0004-9858-9411;
- Zhenwei Xu https://orcid.org/0009-0006-7044-3992;
- Filippo Coletti https://orcid.org/0000-0001-5344-2476.

REFERENCES

BABIKER, O.M., BJERKEBÆK, I., XUAN, A., SHEN, L. & ELLINGSEN, S.Å. 2023 Vortex imprints on a free surface as proxy for surface divergence. *J. Fluid Mech.* **964**, R2.

BIFERALE, L., CHEVILLARD, L., MENEVEAU, C. & TOSCHI, F. 2007 Multiscale model of gradient evolution in turbulent flows. *Phys. Rev. Lett.* **98** (21), 214501.

BOFFETTA, G., DE LILLO, F. & GAMBA, A. 2004 Large scale inhomogeneity of inertial particles in turbulent flows. *Phys. Fluids* **16** (4), L20–L23.

BROCCHINI, M. & PEREGRINE, D.H. 2001 The dynamics of strong turbulence at free surfaces. Part 1. Description. *J. Fluid Mech.* **449**, 225–254.

CANTWELL, B.J. 1992 Exact solution of a restricted Euler equation for the velocity gradient tensor. *Phys. Fluids* A*: Fluid Dyn.* **4** (4), 782–793.

CARDESA, J.I., MISTRY, D., GAN, L. & DAWSON, J.R. 2013 Invariants of the reduced velocity gradient tensor in turbulent flows. *J. Fluid Mech.* **716**, 597–615.

CHEVILLARD, L. & MENEVEAU, C. 2006 Lagrangian dynamics and statistical geometric structure of turbulence. *Phys. Rev. Lett.* **97** (17), 174501.

CHEVILLARD, L., MENEVEAU, C., BIFERALE, L. & TOSCHI, F. 2008 Modeling the pressure Hessian and viscous Laplacian in turbulence: comparisons with direct numerical simulation and implications on velocity gradient dynamics. *Phys. Fluids* **20** (10), 101504.

CHONG, M.S., SORIA, J., PERRY, A.E., CHACIN, J., CANTWELL, B.J. & NA, Y. 1998 Turbulence structures of wall-bounded shear flows found using DNS data. *J. Fluid Mech.* **357**, 225–247.

CRESSMAN, J.R., DAVOUDI, J., GOLDBURG, W.I. & SCHUMACHER, J. 2004 Eulerian and Lagrangian studies in surface flow turbulence. *New J. Phys.* **6** (1), 53.

DAVIDSON, P. 2015 *Turbulence: An Introduction for Scientists and Engineers*. Oxford University Press.

DURHAM, W.M., CLIMENT, E., BARRY, M., DE LILLO, F., BOFFETTA, G., CENCINI, M. & STOCKER, R. 2013 Turbulence drives microscale patches of motile phytoplankton. *Nat. Commun.* **4** (1), 2148.

ECKHARDT, B. & SCHUMACHER, J. 2001 Turbulence and passive scalar transport in a free-slip surface. *Phys. Rev.* E **64** (1), 016314.

ELSINGA, G.E. & MARUSIC, I. 2010*a* Evolution and lifetimes of flow topology in a turbulent boundary layer. *Phys. Fluids* **22** (1), 015102.

ELSINGA, G.E. & MARUSIC, I. 2010*b* Universal aspects of small-scale motions in turbulence. *J. Fluid Mech.* **662**, 514–539.

VAN EMMERIK, T. & SCHWARZ, A. 2020 Plastic debris in rivers. *WIREs Water* **7** (1), e1398.

GEORGE, W.K. & HUSSEIN, H.J. 1991 Locally axisymmetric turbulence. *J. Fluid Mech.* **233**, 1–23.

GIRIMAJI, S.S. & POPE, S.B. 1990 A diffusion model for velocity gradients in turbulence. *Phys. Fluids* A*: Fluid Dyn.* **2** (2), 242–256.

GOLDBURG, W.I., CRESSMAN, J.R., VÖRÖS, Z., ECKHARDT, B. & SCHUMACHER, J. 2001 Turbulence in a free surface. *Phys. Rev.* E **63** (6), 065303.

GYLFASON, A., AYYALASOMAYAJULA, S. & WARHAFT, Z. 2004 Intermittency, pressure and acceleration statistics from hot-wire measurements in wind-tunnel turbulence. *J. Fluid Mech.* **501**, 213–229.

HERLINA, H. & WISSINK, J.G. 2019 Simulation of air–water interfacial mass transfer driven by high-intensity isotropic turbulence. *J. Fluid Mech.* **860**, 419–440.

JÄHNE, B. & HAUSSECKER, H. 1998 Air-water gas exchange. *Annu. Rev. Fluid Mech.* **30** (1), 443–468.

JOHNSON, P.L. 2020 Energy transfer from large to small scales in turbulence by multiscale nonlinear strain and vorticity interactions. *Phys. Rev. Lett.* **124** (10), 104501.

JOHNSON, P.L. 2021 On the role of vorticity stretching and strain self-amplification in the turbulence energy cascade. *J. Fluid Mech.* **922**, A3.

JOHNSON, P.L. & MENEVEAU, C. 2016 A closure for Lagrangian velocity gradient evolution in turbulence using recent-deformation mapping of initially Gaussian fields. *J. Fluid Mech.* **804**, 387–419.

JOHNSON, P.L. & WILCZEK, M. 2024 Multiscale velocity gradients in turbulence. *Annu. Rev. Fluid Mech.* **56** (1), 463–490.

KERR, R.M. 1985 Higher-order derivative correlations and the alignment of small-scale structures in isotropic numerical turbulence. *J. Fluid Mech.* **153**, 31–58.

KOLMOGOROV, A.N. 1941 The local structure of turbulence in incompressible viscous fluid for very large Reynolds numbers. *C. R. Acad. Sci. URSS* **30**, 301–305.

LI, Y., WANG, Y., QI, Y. & COLETTI, F. 2024 Relative dispersion in free-surface turbulence. *J. Fluid Mech.* **993**, R2.

LINDEMANN, C., VISSER, A. & MARIANI, P. 2017 Dynamics of phytoplankton blooms in turbulent vortex cells. *J. R. Soc. Interface* **14** (136), 20170453.

LOVECCHIO, S., ZONTA, F. & SOLDATI, A. 2015 Upscale energy transfer and flow topology in free-surface turbulence. *Phys. Rev.* E **91** (3), 033010.

LOZANO-DURÁN, A., HOLZNER, M. & JIMÉNEZ, J. 2016 Multiscale analysis of the topological invariants in the logarithmic region of turbulent channels at a friction Reynolds number of 932. *J. Fluid Mech.* **803**, 356–394.

LÜTHI, B., HOLZNER, M. & TSINOBER, A. 2009 Expanding the *q*–*r* space to three dimensions. *J. Fluid Mech.* **641**, 497–507.

MCKENNA, S.P. & MCGILLIS, W.R. 2004 The role of free-surface turbulence and surfactants in air–water gas transfer. *Intl J. Heat Mass Transfer* **47** (3), 539–553.

MENEVEAU, C. 2011 Lagrangian dynamics and models of the velocity gradient tensor in turbulent flows. *Annu. Rev. Fluid Mech.* **43** (1), 219–245.

MORDANT, N., CRAWFORD, A.M. & BODENSCHATZ, E. 2004*a* Experimental Lagrangian acceleration probability density function measurement. *Phys.* D*: Nonlinear Phenom.* **193** (1–4), 245–251.

MORDANT, N., LÉVÊQUE, E. & PINTON, J.-F. 2004*b* Experimental and numerical study of the Lagrangian dynamics of high Reynolds turbulence. *New J. Phys.* **6** (1), 116.

MOUNTFORD, A.S. & MORALES MAQUEDA, M.A. 2019 Eulerian modeling of the three-dimensional distribution of seven popular microplastic types in the global ocean. *J. Geophys. Res.: Oceans* **124** (12), 8558–8573.

PAN, Y. & BANERJEE, S. 1995 A numerical study of free-surface turbulence in channel flow. *Phys. Fluids* **7** (7), 1649–1664.

PERRY, A.E. & CHONG, M.S. 1987 A description of eddying motions and flow patterns using critical-point concepts. *Annu. Rev. Fluid Mech.* **19** (1), 125–155.

PETERSEN, A.J., BAKER, L. & COLETTI, F. 2019 Experimental study of inertial particles clustering and settling in homogeneous turbulence. *J. Fluid Mech.* **864**, 925–970.

PUMIR, A., BODENSCHATZ, E. & XU, H. 2013 Tetrahedron deformation and alignment of perceived vorticity and strain in a turbulent flow. *Phys. Fluids* **25** (3), 035101.

QI, Y., LI, Y. & COLETTI, F. 2024 Small-scale dynamics and structure of free-surface turbulence. arXiv:2412.04361.

QI, Y., TAN, S., CORBITT, N., URBANIK, C., SALIBINDLA, A.K.R. & NI, R. 2022 Fragmentation in turbulence by small eddies. *Nat. Commun.* **13** (1), 469.

RUTH, D.J. & COLETTI, F. 2024 Structure and energy transfer in homogeneous turbulence below a free surface. *J. Fluid Mech.* **1001**, A46.

SORIA, J., SONDERGAARD, R., CANTWELL, B.J., CHONG, M.S. & PERRY, A.E. 1994 A study of the fine-scale motions of incompressible time-developing mixing layers. *Phys. Fluids* **6** (2), 871–884.

SREENIVASAN, K.R. & ANTONIA, R.A. 1997 The phenomenology of small-scale turbulence. *Annu. Rev. Fluid Mech.* **29** (1), 435–472.

VERON, F. 2015 Ocean spray. *Annu. Rev. Fluid Mech.* **47**, 507–538.

VIEILLEFOSSE, P. 1982 Local interaction between vorticity and shear in a perfect incompressible fluid. *J. Phys.* **43** (6), 837–842.

VIEILLEFOSSE, P. 1984 Internal motion of a small element of fluid in an inviscid flow. *Physica* A*: Stat. Mech. Appl.* **125** (1), 150–162.

WILCZEK, M. & MENEVEAU, C. 2014 Pressure hessian and viscous contributions to velocity gradient statistics based on gaussian random fields. *J. Fluid Mech.* **756**, 191–225.

XU, H., PUMIR, A. & BODENSCHATZ, E. 2011 The pirouette effect in turbulent flows. *Nat. Phys.* **7** (9), 709–712.

YEUNG, P.K., ZHAI, X.M. & SREENIVASAN, K.R. 2015 Extreme events in computational turbulence. *Proc. Natl Acad. Sci. USA* **112** (41), 12633–12638.

ZHANG, H. 2017 Transport of microplastics in coastal seas. *Estuar. Coast. Shelf Sci.* **199**, 74–86.